Natural Hazards (2022) 114:1585–1608
https://doi.org/10.1007/s11069-022-05439-z

ORIGINAL PAPER

Role of large-scale and microphysical precipitation efficiency on rainfall characteristics of tropical cyclones over the Bay of Bengal

Vijay Vishwakarma[1] · **Sandeep Pattnaik**[1]

Received: 22 February 2022 / Accepted: 30 May 2022 / Published online: 19 June 2022

Abstract

Accurate prediction of rainfall is one of the significant challenges in TC forecasting. In this study, the emphasis is to investigate precipitation efficiency (PE) and associated factors responsible for copious rainfall associated with tropical cyclones (TCs). Two pre-monsoon TCs, i.e., Fani and Yaas, that made landfall over the east coast of India and caused devastation, are considered for this study. Simulation of the TCs was performed using the Advanced Research Weather Research and Forecasting (ARW-WRF) model for up to 96 forecast hours. Results suggest Yass (VSCS), being relatively weaker, TC produced a much higher amount of rainfall compared to Fani (ESCS). The heavy rainfall in Yaas is robustly facilitated by large-scale environmental conditions such as intense low-level vertically integrated moisture flux transport, precipitable water, and low-level convergence. In addition, it is also found that both the large-scale precipitation efficiency (LSPE) and the cloud microphysics precipitation efficiency (CMPE) were significantly higher in the case of Yaas (VSCS), facilitating its intense rainfall characteristics compared to Fani (ESCS). The higher LSPE is regulated by the strong signatures of water vapor flux convergence, atmospheric drying, microphysical consumption of water vapor in the lower part of the troposphere, and gain of solid hydrometeors in the upper troposphere. Overall, the unprecedented intense large-scale moisture transport in Yaas set up a conducive environment for higher precipitation compared to Fani. Our results suggest that the interactions between large-scale environmental systems and local scale precipitation efficiency are key for accurately determining the rainfall and intensification of the TC.

Keywords Rainfall efficiency · Microphysics · Tropical cyclone

✉ Sandeep Pattnaik
spt@iitbbs.ac.in

[1] School of Earth Ocean and Climate Sciences, Indian Institute of Technology Bhubaneswar, Argul, Khurda, Odisha 752050, India

1 Introduction

Precipitation related to a TC is among the most severe weather events which adversely affect the coastal regions where the TC makes landfall. Coastal compound flooding and heavy rainfall from a TC can also trigger vigorous rainfall for the inland regions in a short span of time (Guzman and Jiang 2021). A global climatology of TC has shown a significant contribution to the annual rainfall amounts in a number of regions where TC landfall occurs (Xu et al. 2017), including India. Thus, a rigorous understanding of the physical factors governing the rainfall during TC, its evolution, intensity, and spatial distribution possesses immense socioeconomic relevance. It has been found that precipitation characteristics of a TC strongly influence its intensity (Lonfat et al. 2004), characteristics of the boundary layer (Shapiro 1983; Pattnaik and Krishnamurti 2007), vertical wind shear (Frank and Ritchie 1999, 2001), and interactions of environment with the TC (Jones 1996; Shu and Wu 2009; Konrad and Perry 2010; Shu et al. 2014).

Microphysical processes and synoptic-scale processes depict a closer association with precipitation characteristics of a TC (Kuo 1974; Grell 1993). Although precipitation rate had been found to show a proportional relationship with the intensification of a TC and cumulus parameterization of water vapor convergence in the previous studies (Fristch and Chappel 1980; Grell 1993; Pattnaik et al. 2011; Baisya et al. 2020), the total available moisture flux or condensation is not used in the making of precipitation which is subject to the relationship between rainfall rate incoming water vapor flux, raindrops re-evaporation, moistening of local atmosphere and loss of hydrometeors at different levels (Doswell et al. 1996; Lau and Wu 2004). So as to study the rain-bearing capacity of intense weather systems such as TCs, quantification of PE is proposed (Braham 1952). Initial studies on PE have shown that PE is an important parameter that incorporates both the surface precipitation related to cloud microphysical processes and large-scale water vapor convergence (Auer and Marwitz 1968; Sui et al. 2005, 2007; Xu et al. 2017). In the previous studies of PE (Lipps and Hemler 1986; Li et al. 2002), it has been defined as the ratio of surface precipitation to all the precipitation sources. Further, PE is categorized into LSPE and CMPE, where LSPE is the ratio of surface rain rate to the net moisture convergence rate (Fankhauser 1988) and CMPE is the ratio of the surface rain rate to the sum of condensation and deposition rate (Weisman and Klemp 1982; Ferrier et al. 1996). LSPE and CMPE can be non-negative and greater than 100% (Sui et al. 2005). They have been widely used to investigate the precipitation characteristics of intense weather systems (Hobbs et al. 1980; Heymsfield and Schotz 1985; Hanesiak et al. 1997), i.e., storms and heavy rainfall events over the tropics as well as extra-tropics (Carbone 1982; Chong and Hauser 1989; Cotton et al. 1989).

Since the initial studies of PE (Braham 1952; Palmen and Newton 1969), it has been found that PE has a closer relationship with the total available water vapor of rain-bearing weather systems (Sui et al. 2007). It shows that PE is an important physical parameter that combines surface precipitation with microphysical processes related to cloud and water vapor convergence on a large-scale. Modulation of PE by other physical factors is found to be related to vertical wind shear (Fankhauser 1998) and entrainment rate affecting the saturation of air parcel, bringing the environmental air inside the cloud (Doswell et al. 1996). Among the other favorable environmental factors, ambient precipitable water, increased water-vapor supply and longer residence time of raindrops contribute positively to PE (McCaul et al. 2005; Krishbaum and Grant 2012). Prediction of extreme rainfall during intense weather events such as TC has noted the significant contribution of microphysical characteristics of precipitation (Bell 2017), and recent studies of high rainfall accumulations in the events show that high-resolution mesoscale models can obtain good quantitative forecast skills for even the larger rainfall thresholds (Wang 2015; Chakraborty et al. 2021). However, numerical weather prediction models are still showing a threshold for their sensitivity and uncertainties of the cloud microphysics in the parameterization (Hendricks et al. 2016). The challenge of eliminating the uncertainties is largely due to the lack of microphysical observations related to TCs (Brown et al. 2016), particularly over the NIO basin. However, recent technological improvements in observation systems have shown great promise in helping to validate and improve parameterizations of rain processes.

Previous studies on the PE related to storms (Sui et al. 2005, 2007) over Atlantic and Pacific basins have been carried out (Gao and Li 2011), but similar research on the PE of TC is not been carried out over the NIO basin, which accounts for about 7% of intense global TC and they are deadliest in nature (Balaji et al. 2018). Thus, some of the important questions still remain unanswered for the TCs of the NIO basin. In this study, two cases of TC are considered, i.e., an extremely severe cyclone (Fani) and a very severe cyclonic storm (Yaas) that evolved over the NIO basin during pre-monsoon season and caused socioeconomic loss along the east coastal region of India, including the state of Odisha and West Bengal.

The present study aims to a better understanding of the microphysical and large-scale characteristics of precipitation and to investigate the physical processes responsible for the contrasting heavy rainfall events that occurred during the TCs Fani (2019) and Yaas (2021). Specifically, the conceptualization of this study is based on two key questions, i.e., a) What are the dominant local and large-scale factors responsible for intense rainfall situations during TCs? (b) How is PE being regulated through complex dynamical and thermodynamical processes of the TCs? The overall organization of the paper is as follows, i.e., introduction (Sect. 1), synoptic description of TCs Fani and Yaas (Sect. 2), model and methodology (Sect. 3), results, and discussions (Sect. 4), followed by conclusions (Sect. 5).

2 Synoptic description of Fani (2019) and Yaas (2021)

On 26 April, 2019, a depression located to the west of Sumatra was tracked by India Meteorological Department (IMD). Afterward, the system slowly coalesced while moving northward and was upgraded to a deep depression at 0000 UTC 27 April. IMD named the system as storm "Fani" as it upgraded to a cyclonic storm after six-hour. The convection around the system was waned and waxed, and Fani continued to intensify until 1800 UTC 27 April, after which it remained stagnant for over a day. IMD categorized the TC as a severe cyclonic storm when Fani resumed strengthening around 1200 UTC. Under very favorable environmental conditions with sea surface temperature of 30–31 °C and low vertical wind shear, IMD noted a rapid intensification of the TC. Afterward, IMD upgraded the system to a very severe cyclonic storm around 0000 UTC on 30 April. With tight spiral banding wrapping into a formative eye feature, the organization of the system improved, and IMD upgraded the TC to an extremely severe cyclonic storm around 1200 UTC. Afterward, the development of the system slowed down, and shortly after 0600 UTC on 02 May, another period of rapid intensification, attaining 1-min sustained winds of 280 km/hr was observed (IMD 2019). Further, Fani quickly weakened after its peak intensity, and it made its landfall as an extremely severe cyclonic storm near Puri, Odisha, at 0230 UTC 03 May, with maximum 3-min sustained wind of 185 km/hr. In this way, Fani came to be one of the most intense TCs making landfall over the east coast of India.

On 22 May 2021, a low-pressure area formed over the east-central Bay of Bengal (BoB). Over the same region, it lays as a well-marked low-pressure area (WML) at 0900 UTC 22 May 2021. It concentrated into a depression over the east-central BoB under a favorable environment at 06 UTC 23 May 2021. Further, it translated north-westwards and intensified into a deep depression (DD) over east-central BoB at 1800 UTC May 23, and IMD upgraded the system into a cyclonic storm and named it as storm "YAAS" at 0000 UTC 24 May over the same region. While translating north-north-westwards it intensified into a severe cyclonic storm around 1800 UTC 24 May. Further it moved northwards from the 0300 UTC 25 May and intensified into a very severe cyclonic storm (VSCS) at 1200 UTC over northwest BoB. Further, it reached a peak intensity of 138.9 km/hr and was located over northwest BoB about 30 km east of Dhamra Port, Odisha, around 0000 UTC 26 May. While translating toward the north-north-westward, it crossed the Odisha coast about 20 km to the south of Balasore, Odisha, as VSCS with maximum sustained wind speed (MSW) up to 130–140 km/hr and gusting up to 155 km/hr around 0500-0600 UTC 26 May. Further, moving north-north-westward, it weakened into a depression over central parts of Jharkhand at 0600 UTC 27 May. Apart from producing very heavy rainfall and squally winds in its formative stage, it caused heavy to extremely heavy rainfall at isolated places over coastal Odisha on 25 May and heavy to very heavy rainfall at a few places, and extremely heavy rains at isolated places on 26 May over north Odisha. Further, it has also caused heavy to very heavy rainfall activity at isolated places over Gangetic West Bengal on 26 May and heavy to extremely heavy rainfall over Sub-Himalayan West Bengal on 27 May (IMD 2021). It also caused heavy to extremely heavy rainfall over Jharkhand on 26 and 27 May, over Bihar and east UP on 27 and 28 May. Both these cyclones occurred during the pre-monsoon season over the Bay of Bengal and made landfall in Odisha (the eastern coast of India) but put enormous challenges to the forecasting agencies to accurately predict its characteristics, i.e., intensity, track, and rainfall with adequate lead time. Keep these factors in view, these two cyclones are considered in this study.

3 Model and methodology

3.1 Model

The WRF-ARW 4.0 version model (Skamarock et al. 2008) is used to conduct experiments with two-way interactive doubly nested domains having horizontal resolutions of 9 and 3 km (Fierro et al. 2009; Rai and Pattnaik 2018; Rai et al. 2019). The model has 53 vertical levels, with the top fixed at 50 hPa. The model integration starts at 0000 UTC 29 April 2019 and ends at 0000 UTC 03 May 2019 for Fani and 0000 UTC 23 May 2021, and ends at 0000 UTC 27 May 2021 for Yaas, and this duration has been selected to emphasize rainfall characteristics, particularly during landfall. The initial and boundary conditions for the simulations are obtained from the National Centers for Environmental Prediction (NCEP) Global Forecast System (GFS) forecast data with a horizontal resolution of 0.25×0.25° at 6-h intervals. The model physics options include Kain–Fritsch (Kain 2004) cumulus for the outer domain (9 km), inner domain (3 km) is explicitly resolved (Ooyama et al. 1982). Detailed model configurations are mentioned in Table 1. The SST obtained from National Oceanic and Atmospheric Administration (NOAA) 0.25×0.25° daily optimum interpolation Sea Surface Temperature

Table 1 WRF 4.0 model configuration details

	Parent domain	Inner domain
Horizontal resolution	9 km	3
Vertical levels	53	53
Forecast length	96 h	96 h
Time step	30 s	10 s
Model forecast output time interval	6 hourly	1 hourly
Planetary boundary layer	Bougeault–Lacarrere Scheme (BouLac) (Bougeault et al. 1989)	
Microphysics	WRF Double Moment 6–class Scheme (Lim et al. 2010)	
Long-wave radiation	CAM (Collins et al. 2004)	
Short-wave radiation		
Surface layer	MM5 Similarity scheme (Paulson 1970)	
Land surface	Unified Noah land-surface model (Tewari et al. 2004)	
Cumulus	Kain-Fritsch Scheme (Kain 2004)	Explicitly resolved
SST(daily): OI SST		
Initial and Boundary conditions(6 hourly): GFS		

(OISST) is updated at 6 hourly intervals (Mogensen et al. 2012). Additional detailed information about model configuration and SST are presented in Tables 1 and 2, respectively. All the simulation configurations are identical and integrated up to 96 h lead time from their respective initial conditions. The IMD best track, translational speed (TS) and intensity, i.e., 10-m maximum sustained wind (MSW) and minimum central pressure as (MCP), and Global Precipitation Measurement (GPM) 10 km resolution precipitation data (Huffman et al. 2015) are used to validate the model forecast results. All the results discussed are for the innermost domain (3 km).

3.2 Methodology

PE can be divided into two broad categories, i.e., LSPE and CMPE, on the basis of its calculation method. Large-scale environmental conditions are shown by LSPE, and microphysical processes are shown by CMPE. PE and its individual contributing terms have been calculated as per the following equations (Gao et al. 2005; Lim et al. 2010; Campos and Wang 2015)

$$P_s = Q_{\mathrm{WVT}} + Q_{\mathrm{WVF}} + Q_{\mathrm{WVE}} + Q_{\mathrm{CM}} \quad (1)$$

Table 2 Experimental design

S. no	Experiment name	Details of the experiment
2	Fani	OI SST (0.25 × 0.25°) updated at 6 h interval
3	Yaas	OI SST (0.25 × 0.25°) updated at 6 h interval

$$P_s - Q_{CM} = Q_{WVS} \tag{2}$$

$$Q_{WVT} + Q_{WVF} + Q_{WVE} = Q_{WVS} \tag{3}$$

$$P_s = \overline{\rho}\left(w_{T_r} q_r + w_{T_r} q_s + w_{T_r} q_g\right) \tag{4}$$

$$Q_{WVT} = -\frac{\partial[q_v]}{\partial t} \tag{5}$$

$$Q_{WVF} = -\left[\frac{\partial(uq_v)}{\partial x} + \frac{\partial(vq_v)}{\partial y}\right] \tag{6}$$

$$Q_{WVE} = E_s \tag{7}$$

$$Q_{CM} = -\frac{\partial[q_5]}{\partial t} - \left(\frac{\partial[uq_5]}{\partial x} + \frac{\partial[vq_5]}{\partial y}\right) \tag{8}$$

where

$$q_5 = \{q_c, q_r, q_i, q_s, q_g\} \tag{9}$$

$$\text{LSPE} = P_s / \left(H(Q_{WVT})Q_{WVT} + H(Q_{WVF})Q_{WVF} + Q_{WVE} + H(Q_{CM})Q_{CM}\right) \tag{10}$$

$$\text{CMPE} = P_s / \left(H(Q_{WVS})Q_{WVS} + H(Q_{CM})Q_{CM}\right) \tag{11}$$

where P_S represent the surface rain rate and it is equal to the sum of the vapor processes, which involves local atmospheric drying or moistening (Q_{WVT}), vapor flux convergence or divergence (Q_{WVF}), surface evaporation (Q_{WVE}), and cloud-related processes, including hydrometeor loss/convergence or hydrometeor gain/divergence (Q_{CM}); microphysical consumption of net water vapor has been designated by Q_{WVS}, the average atmospheric density (ρ); rain, snow, and graupel terminal velocities (wTr, wTs, wTg); water vapor mixing ratio, cloud water, rainwater, cloud ice, snow and graupel (q_v, q_c, q_r, q_i, q_s, q_g); the zonal and meridional components wind (u, v); and the surface evaporation (E_S). The required variables have been obtained from the WRF model output, and they are used in the calculation of the above-mentioned parameters. $[()] = \int_{z_b}^{z_t} \rho()dz$ Represents the vertically integrated variable in the air column by mass, where z_t and z_b show the top and bottom height of the atmosphere, respectively. While calculating LSPE and CMPE all the negative values of Q_X have been left out so that we could have a positive value of PE. Positive values of Q_X are shown by $H(Q_X)Q_X$ in the above equations (Sui et al. 2005).

4 Results and discussions

In this section, a detailed analysis of the two simulated storms, e.g., Fani and Yass are presented in terms the storm's track, intensity (maximum sustained wind (MSW) and minimum central pressure (MCP), rainfall, vertical updraft, radial, and tangential wind, low-level convergence, diabatic heating, vertically integrated moisture transport, liquid (e.g., cloud water rainwater) and frozen (e.g., graupel, snow, ice) hydrometeors and precipitation efficiency and its individual terms. The radial distribution of some of the parameters is analyzed over 300 km from the storm center for the respective forecast hours (up to 96 h). These analyses are carried out to provide further insight into key processes competing at finer scales as well as the large-scale impacting characteristics and modulating the rainfall of the TCs. Apart from these parameters, a schematic depicting the competence of processes is presented to quantify and interlink the relative contribution of these dominant processes regulating rainfall and other characteristics of TC.

4.1 Track and intensity

The observed (IMD) and simulated tracks up to 96 forecast hours for Fani and Yaas are shown in Fig. 1a, b and Fig. 2a–d, respectively. In general, TCs over BoB emerge from low-pressure systems in the equatorial India Ocean and migrate northward, and this is evident from the respective tracks (Krishna 2009; Ng and Chan 2012). The simulated track of Fani is able to capture the initial northwest-ward followed by eastward curvature, which brings it closer to the IMD; however, in the case of Yaas, the simulated track has deviated from the observed track during initial forecast hours (Up to 24 h). As the forecast proceeds beyond 24 h, the forecast is able to capture the observed track for Yaas. This minor deviation during the initial 24 h forecast in Yaas compared to Fani is mainly due to the model spin-up of the issue. Fani is a more organized TC compared to Yaas, facilitating fewer

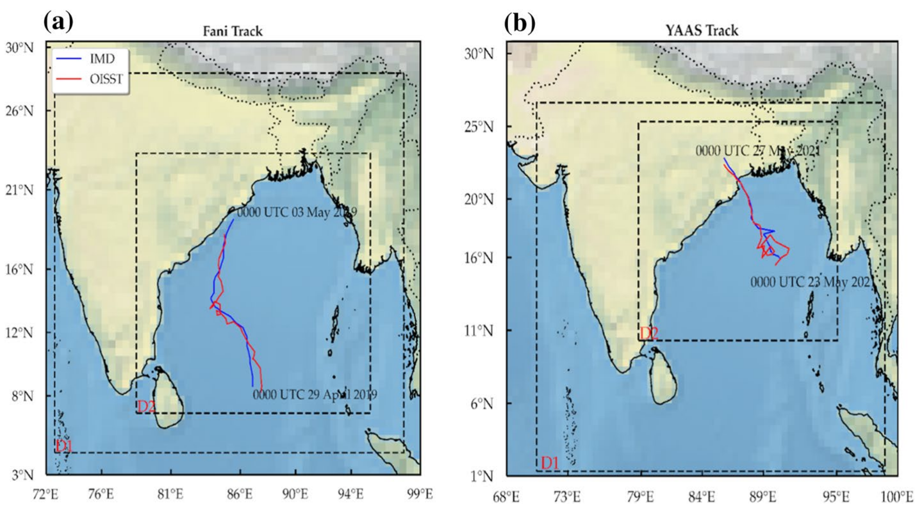

Fig. 1 Observed (IMD) and simulated storm tracks of **a** Fani (IC: 0000 UTC April 29 2019–0000 UTC May 03 2019) and **b** Yaas (IC: 0000 UTC May 23 2021–0000 UTC May 27 2021) throughout the 96 forecast hours

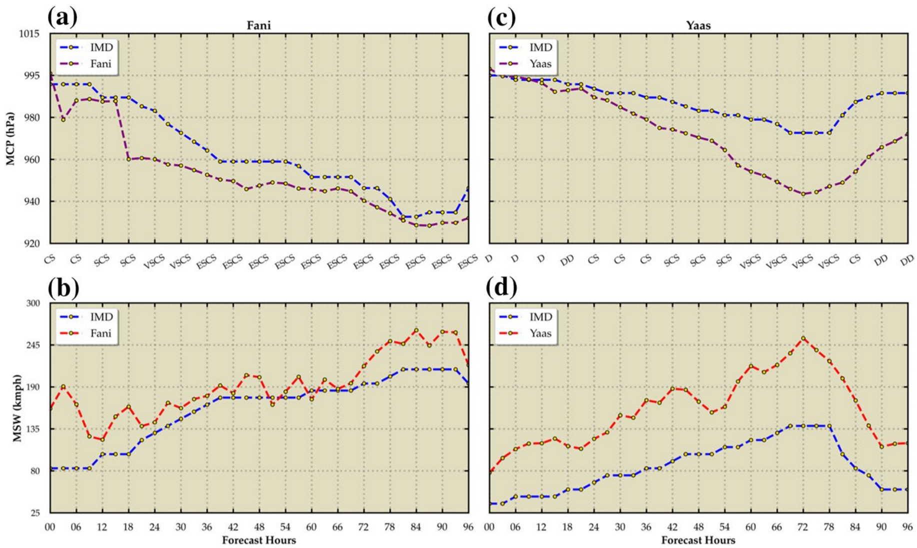

Fig. 2 Observed (IMD) and simulated MCP (hPa) and MSW (kmph) for Fani **a**–**b** and Yaas **c**–**d**

spin-up errors. The overall model captures the forecasted tracks for both the TCs reasonably well compared to IMD, suggesting the model forecasts products are robust for further diagnostics.

The forecast intensity up to 96 h in terms of MSW and MCP are presented in Fig. 2a–d. The simulated intensities in terms of MSW (MCP) of both the TCs have shown marginal over (under) estimation throughout the forecast hours, but the overall intensity forecast is better captured in the case of Fani as compared to Yaas. Initially (i.e., up to 24 h), the difference of MCP is larger about 11.3 hPa (smaller, 1.2 hPa) in the case of Fani (Yaas) compared to IMD; however, as the forecast hour proceeds, the magnitude of difference in Yaas (Fani) gradually increases and with maximum difference up to 20 hPa against IMD. It is evident from Fig. 2b, d that both the TCs have a rapid intensification (RI) phase 24 h prior to their peak phases (Kaplan and DeMaria 2003). The magnitude of RI for Fani (IMD) is 74.08 (60.89 km/hr, 12–36 h), and in the case of Yaas (IMD), it is 68.90 (55.56 km/hr, 42–76 h). In general, it is noted that despite TC Fani being more intense (i.e., ESCS) than Yaas (i.e., VSCS), the rate of intensification in both of these systems are quite similar, with Fani having little more (i.e., 6 km/hr) intensified. This is to highlight that even though their rate of intensification is similar there are large differences between these two in terms of rainfall and associated processes. That is the major focus area of this research work. In this aspect, rigorous analyses are carried out in terms of rainfall distribution, rainfall efficiency, and key mechanisms regulating the TC precipitation characteristics in the following sections.

4.2 Rainfall

This section quantifies the model forecasted 24 hourly accumulated rainfall associated with these two TCs, including their respective intensification stages. The GPM and forecasted rainfall are shown in Fig. 3a–p. In general, it is noted that both Fani and Yaas have produced intense rainfall (> 100 mm/hr) with spatial extent up to 300 km

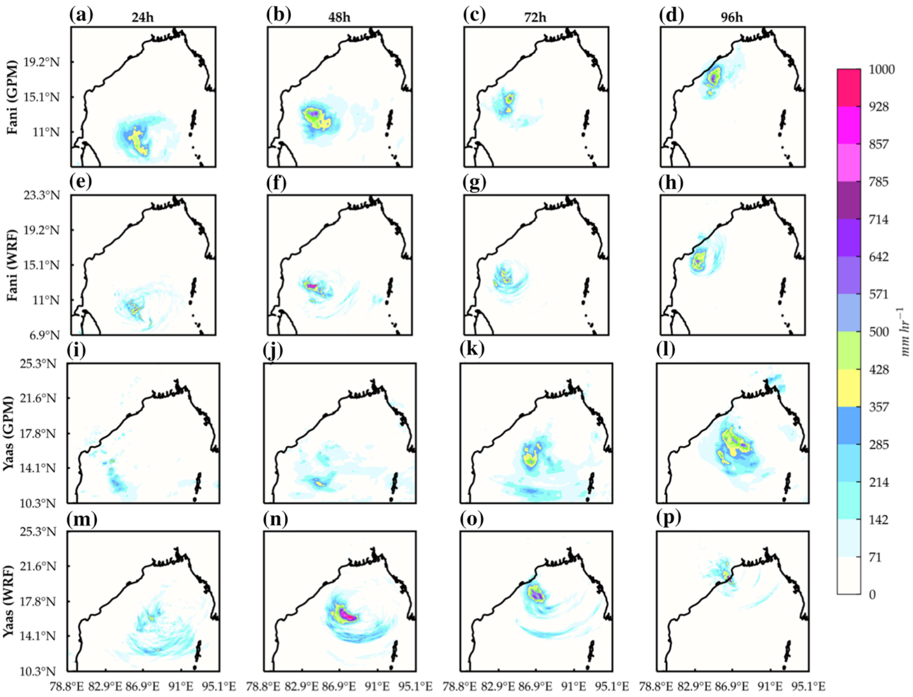

Fig. 3 Observed (GPM) and simulated 24 hourly accumulated rainfall (mm/hr) for Fani (**a**–**h**) (IC: 0000 UTC April 29 2019–0000 UTC May 03 2019) and Yaas (**i**–**p**) (IC: 0000 UTC May 23 2021–0000 UTC May 27 2021)

radii from its center throughout the forecast duration (i.e., up to 96 h). It is interesting to note that, in the southwestern sectors of the TCs, there is a large surplus > 50 mm/hr compared to GPM. In general, model forecasts (Fani and Yaas) have shown slight overestimation against the observed rainfall (GPM); they are able to capture the rainfall evolution and its structure skilfully throughout the forecast hours (Fig. S2 a–p). However, it is noted that the forecasted precipitation for both the TCs, particularly during the last 24 h (72–96 h), was underestimated (i.e., 30 mm/hr for Fani, 50 mm/hr for Yaas).

In contrast to the gradual increment of accumulated rainfall with the forecast hour due to intensification, it is also noted that both the rainfall amount and distribution in the case of Fani (Fig. 3a–h) are relatively moderate and over a limited region as compared to Yaas (Fig. 3i–p). One of the factors for the limited distribution of the rainfall in Fani might be attributed to the more organized and intensification (ESCS) of the system compared to Yaas. But beyond this limited generic inference, there are some more depth attributes that need to be elucidated. Therefore comprehensive analyses are carried out to understand the key mechanisms (e.g., vertical updraft, diabatic heating, moisture flux transport, precipitable water, including rainfall efficiency) behind the typical and contrasting characteristics of rainfall in each of these pre-monsoon TCs (i.e., Fani and Yaas) in the following sections.

4.3 Dynamical and thermodynamical processes

In this section, important dynamical and thermodynamical features of the TCs are discussed throughout the 96 forecast hours, including their RI intensity phases. The composite analysis in terms of azimuthally averaged vertical mean structure up to 300 km from the respective centers of the TCs at 1-h intervals is presented. The purpose of these analyses is to capture and identify the distinct signatures of core and large-scale processes during different phases of the TC (i.e., developing and mature), with distinct signatures of rainfall. The mean structures in terms of pressure-time cross-section analysis of diabatic heating, radial, and tangential wind are shown in Fig. 4a–f. Further, radial and tangential wind components are calculated using the following momentum equations (Eqs. 12 and 13) in the cylindrical coordinate system (r, θ, z) (Xu and Wang 2010a):

$$\frac{\partial u}{\partial t} + u\frac{\partial u}{\partial r} + \frac{v}{r}\frac{\partial u}{\partial \theta} w\frac{\partial u}{\partial z} - \frac{v^2}{r} - fv = -\frac{1}{\rho}\frac{\partial p}{\partial r} \tag{12}$$

$$\frac{\partial v}{\partial t} + u\frac{\partial v}{\partial r} + \frac{v}{r}\frac{\partial v}{\partial \theta} w\frac{\partial v}{\partial z} - \frac{uv}{r} + fv = -\frac{1}{\rho}\frac{\partial p}{\partial r} \tag{13}$$

where u, v, and w are the radial, tangential, and vertical components of the wind, cylindrical coordinates r is the radius from the TC center pointing outward, θ is an azimuthal angle, and z is the height along the vertical axis, and p, and ρ are atmospheric pressure and density, respectively. Diabatic heating from the model output has been calculated using the following equations (Yanai et al. 1973):

$$s = c_p T + gz \tag{14}$$

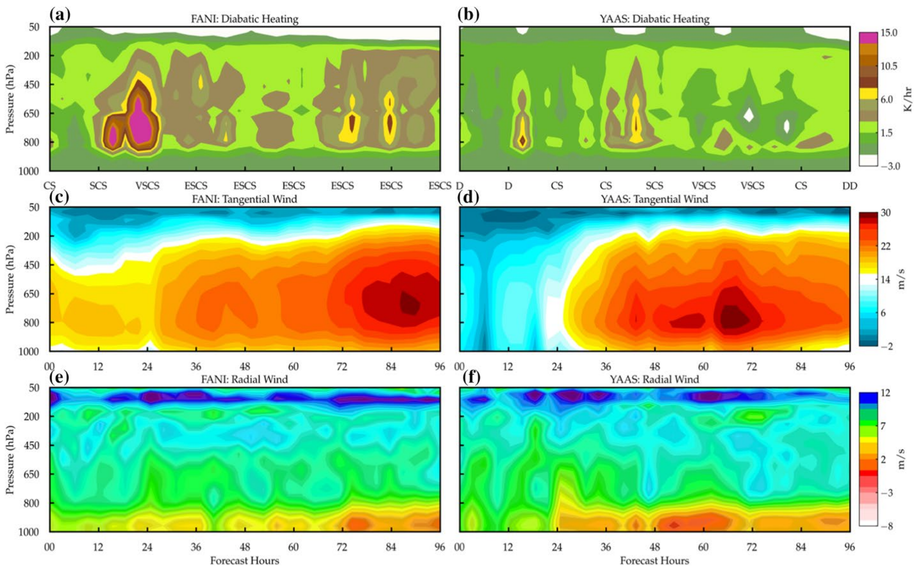

Fig. 4 Fani and Yaas time-pressure cross section of (**a**–**b**) diabatic heating (K/h), (**c**–**d**) tangential wind (m/s), and (**e**–**f**) radial wind (m/s) during 96 forecast hour

$$Q_1 = \frac{\partial \bar{s}}{\partial t} + \bar{v}.\nabla \bar{s} + \omega \frac{\partial \bar{s}}{\partial p} \tag{15}$$

$$Q_1 = Q_R + L(c - e) - \frac{\partial \overline{s'\omega'}}{\partial p} \tag{16}$$

where Q_1, Q_R, s,c_p, T, g, z, L, c, e, v, ω, and p represent diabatic heating, radiative heating, dry static energy, the specific heat capacity of air at constant pressure, temperature, acceleration due to gravity(9.8 m/s^2), altitude (m), latent heat of vaporization of liquid water (J/Kg), rate of condensation per unit mass of air, rate of re-evaporation of cloud droplets, horizontal wind (m/s), vertical wind and pressure (hPa), respectively. Variables with bar and prime sign designate the mean and perturbation value, respectively, over the considered time period.

In Fig. 4a, b, the pressure-time cross section of diabatic heating (K/hr) is shown. It is noted that Fani has strong diabatic heating (13–15 K/hr) around 24 forecast hours compared to Yaas (6–8 K/hr). Such intense heating might result due to the low shear zone facilitating intensification due to the vertical stretching (Hazelton et al. 2017; Yang et al. 2019). Beyond 24 h, both the TCs have shown a decrement in the diabatic heating. Yaas has shown a rapid decrease in heating (−3 K/hr), whereas this decrement is gradual in the case of Fani (~1.5 K/hr) just after the peak phases of TCs. It is clearly seen that diabatic heating has played a dominant role in the intensification process of TC, leading to Fani as ESCS and Yaas as VSCS. Additionally, the diabatic heating process supports the deep convection, vortex strengthening, and eyewall development, resulting in the RI (Fig. 2b, d) in both the TCs (Hazelton et al. 2017).

Figure 4c, d shows the pressure-time cross section of tangential wind for Fani and Yaas throughout the forecast duration. In the case of Fani, the strong tangential wind is noted as compared to Yaas, and the maxima of tangential wind for Fani (Yaas) reaches up to 30 (30 m/s), designating the eyewall development during their respective peak phases. It is also noted that the intensification of tangential wind has been gradual in Fani (~60 h) as compared to a sharp increment in Yaas (~36 h). This contrasting intensification is among one of the key dynamic signatures leading to more intense TC Fani (ESCS) compared to Yaas (VSCS). Radial wind depicts similar structures for both the TC and is coherent with the structure of tangential wind (Fig. 4e, f). Maxima of radial wind for Fani (Yaas) reaches up to 12 (12 m/s) during their respective peak phases. These results support that an accurate forecast of tangential and radial wind components in TC is also essential to facilitate its intensification process.

4.4 Vertical updraft and Hydrometeors

In Fig. 5a–c, column integrated (1000–50 hPa) vertical updraft (only upward velocity) and hydrometeors (i.e., cloud water, rainwater, ice, snow, and graupel) are presented within 300 km radii from the center of TC. During the initial forecast hour (3 h), a strong vertical updraft (25 cm/s) is noted for Fani, whereas it is relatively weaker in the case of Yaas (10 cm/s). This updraft, designating a measure of convection, reaches the maxima 18 (20 cm/s) around 30 h for both the storms Fani (Yaas). Around 51 h, a sharp (gradual) decrease in updraft for Fani (Yaas) reaching up to 7 (10 cm/s) is noted. Afterward, a persistent updraft > 10 cm/s in the case of Fani is noted till the end of the forecast hour, whereas Yaas has shown a gradual decrease and reached a strength of 6 cm/s around 96 h. This

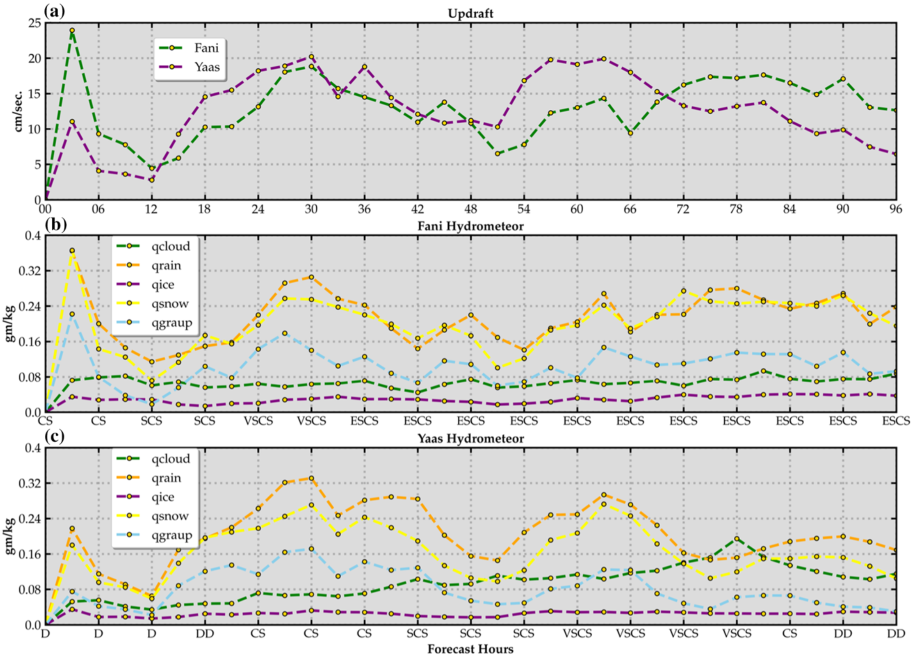

Fig. 5 Fani and Yaas simulated **a** updraft (cm/s) and (**b**–**c**) hydrometeor (gm/kg) during 96 forecast hour

suggests that Yaas is relatively weakened compared to Fani as it is approaching the coast during the landfall (90 h). This is interesting as a relatively weaker TC (i.e., Yass) has produced much larger rainfall compared to intensified TC (i.e., Fani).

The hydrometeors (i.e., cloud water, rainwater, ice, snow, and graupel) for both the TCs are presented in Fig. 5b, c. During the initial forecast hours (up to 12 h), quantitative distribution of all hydrometeors markedly dominates in Fani, except ice which remains almost constant throughout the forecast period. After 12 h, rain, snow, and graupel has shown a gradual (sharp) rise in case of Fani (Yaas) and reaching up to 0.3 (0.32 g/kg), 0.25 (0.27 g/kg), and 0.12 (0.16 g/kg), respectively, around 30 forecast hour. Further, Fani (Yaas) has shown a gradual (sharp) decrease in the hydrometeors up to 51 h for rain, snow, and graupel reaching 0.17 (0.14 g/kg), 0.1 (0.09 gm/kg), and 0.08 (0.05 gm/kg), respectively. After 51 h, Fani (Yaas) has shown gradual (sharp) increment reaching up to 0.29 (0.27 g/kg), 0.27 (0.26 g/kg), and 0.13 (0.12 g/kg) during their respective peak phases 72 (60 h), finally Fani (Yaas) has shown a gradual (sharp) decrement up to the last 96 forecast hours. A closer resemblance of updraft and hydrometeor pattern suggests that the former being conducive for the later and conclusively Fani (Yaas) depicting gradual (sharp) changes of the distribution of these variables has led to the moderate (enhanced) rainfall. Overall, we have noted that the whole tendency of vertical updraft resembled that of hydrometeors, and the maximum value appeared during their peak intensification phase. In the case of Fani, updrafts are either strong or closer to Yaas; however, there is a weaker distribution of hydrometeors in the case of Fani compared to Yaas. This suggests moderate convection along with abundant hydrometeors has augmented the rain-making processes, and it is being manifested as intense rainfall in the case of Yaas. More supportive results and discussions are presented in the following section.

4.5 Moisture flux transport and precipitable water

In this section, large-scale processes in terms of vertically integrated moisture flux transport (VIMFT) and precipitable water has been analyzed and presented for the outer domain 9 km (Fig. 1a, b) of TCs. This is due to the influence of large-scale factors, as discussed in this section. The VIMFT is calculated using the following equation Fasullo and Webster (2002):

$$\text{VIMFT} = -\frac{1}{g}\int_{1000hPa}^{700hPa} q\vec{U}dp \tag{17}$$

where g, p, q, and $\vec{U}$ are the acceleration due to gravity, pressure, specific humidity, and wind (m/s), respectively. Calculation of VIMFT is performed in the lower level of the troposphere (1000–700 hPa) where the maximum proportion of water vapor transport occurs (Huang et al. 2015).

Precipitable water (PWT) has been calculated using the following equation (Gao et al. 2017):

$$\text{PWT} = -\frac{1}{g}\int_{1000hPa}^{50hPa} qdp \tag{18}$$

VIMFT for Fani and Yaas is shown in Fig. 6a–h at 24-h intervals up to 96 h. During the initial 24 h, VIMFT ranges from 300 to 1500 kg/m/s for both the TCs. However, it has a wider spatial extent in the case of Yaas compared to Fani. As the forecast proceeds beyond 24 h, gradual (sharp) increment in the case of Fani (Yaas) is noted, which shows VIMFT up to 2400 (kg/m/s) around 48 h. Afterward, an even more pronounced sharp(gradual)

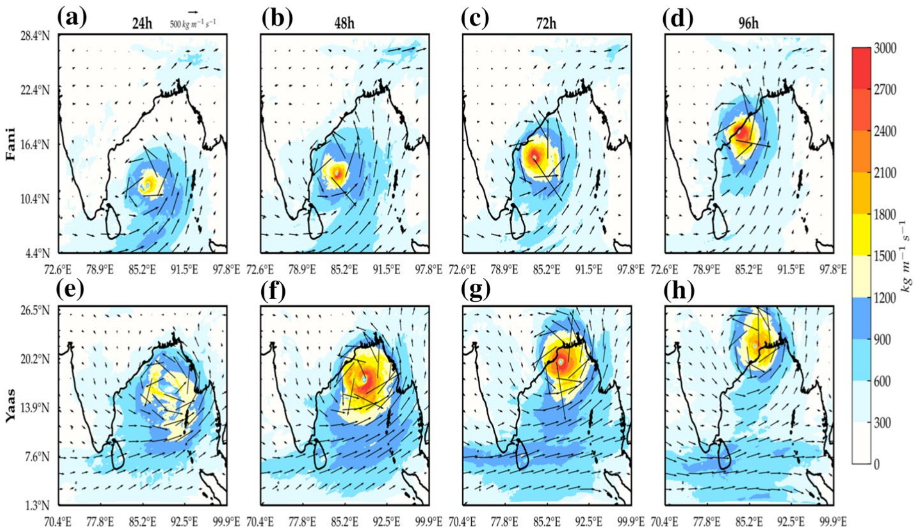

Fig. 6 Simulated moisture flux transport (kg*m^{-1}*s^{-1}) for Fani (**a**–**d**) (IC: 0000 UTC April 29 2019–0000 UTC May 03 2019) and Yaas (**e**–**h**) (IC: 0000 UTC May 23 2021–0000 UTC May 27 2021) during 96 forecast hour

increase in VIMFT in the case of Fani (Yaas) is noted till the end of their respective peak intensification phases(12–36 h for Fani and 42–76 h for Yaas) and it has shown VIMFT up to 3000 kg/m/s near the eyewall region. In the last 96 h, Yaas has shown a sharp decrement where VIMFT has shown a value upto 1200–2100 kg/m/s near the eyewall region, whereas Fani has shown a value 1200–2400 kg/m/s. This suggests wider spatial extent and sharp changes of VIMFT in the case of Yaas are more prominent as compared to Fani. It is again supporting our hypothesis that in spite of Fani (ESCS) being more intense as compared to Yaas (VSCS), the latter one experiencing more rainfall can be attributed to the larger spatial extent of VIMFT values (~3100 kg/m/s) and sharp changes as compared to the former one.

PWT at a 24-h interval is presented for domain-2 (9 km) in Fig. 7a–p. It is noted that Yaas has produced intense PWT (>50 mm) as compared to Fani throughout the forecast duration. For both, the TCs maxima of PWT reach during their respective peak intensification phases. During the initial 24 h, PWT for Fani and Yaas ranges from 75 to 81 mm. As the forecast proceeds beyond 24 h, a gradual (pronounced) increment up to 81 mm is noted in the case of Fani (Yaas) around 48 h. Afterward, the increment in PWT becomes less (more) well-marked for Fani (Yaas) around 72 h, and it reaches a value up to 88 mm, which corresponds to their respective peak phase of intensification. In the last 96 h, Fani (Yaas) has shown a gradual decrease in PWT and reached PWT up to 75–81 mm. Overall there is a sharp increment in PWT in Yaas compared to Fani. The main reason attributed to these results is that Yaas occurred around the same time as the establishment of monsoon low-level jet over the NIO. It is evident that stronger low-level jet induced pumped in more VIMFT (Fig. 6e–h) and PWT (Fig. 7a–p) in turn facilitated by stronger updrafts with lower-level convergence (Fig. S1b), leading to a large accumulation of cloud hydrometeors (Fig. 5a–c) formation led to copious rainfall in the case of Yaas. Interestingly, besides the presence of large-scale moisture flow, this fact is again re-establishing in the following section when precipitation efficiency and associated terms are discussed in terms of contributing to very high rainfall in Yaas compared to Fani.

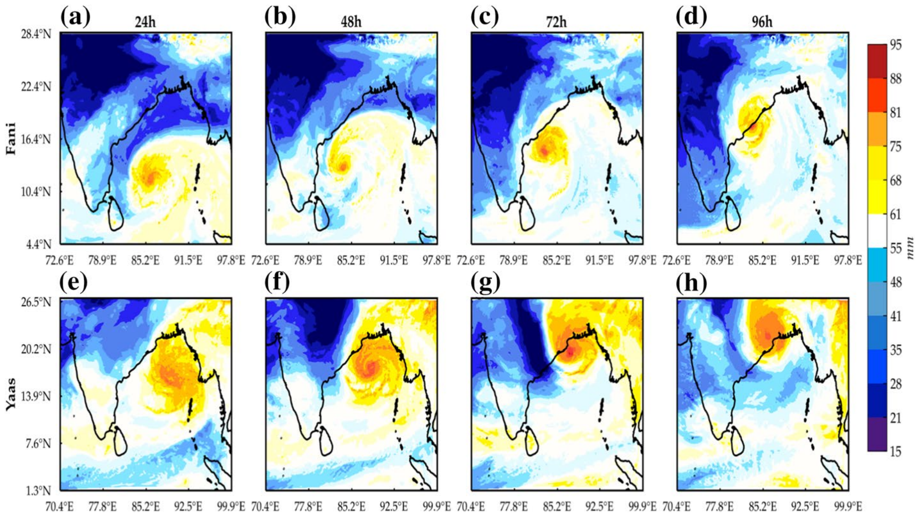

Fig. 7 Simulated precipitable water (mm) for Fani (**a**–**d**) (IC: 0000 UTC April 29 2019–0000 UTC May 03 2019) and Yaas (**e**–**h**) (IC: 0000 UTC May 23 2021–0000 UTC May 27 2021) during 96 forecast hours

4.6 Precipitation efficiency

To further analyze the differences in cloud microphysical characteristics, we have focused our analysis on the region of 300 km from the center of the storm. Based on the methodology discussed in Sect. 3.2, precipitation efficiency and its individual terms are shown in Fig. 8a, d and Fig. 9a, d for Fani and Yaas, respectively. Figure 8a, c shows the radially averaged time-series of rain rate, LSPE, and CMPE for the TCs Fani and Yaas. It is noted that for Fani (Yass), the forecasted rain rate of 80 (110 mm/hr) is skillfully represented against their respective observed values 78 (115 mm/hr) forecast hours at 51 (33 h). Further, it is also noted that the rain rate maxima for Fani (Yaas) are 108 (155 mm/hr) during their respective peak intensification phase against the observed rain rate of 90 (115 mm/hr). Fani at this stage is ESCS, and Yaas is SCS, and landfall has not occurred in any of these TCs. Results also suggest that after 54 h (36 h) in Fani (Yaas), there is a distinct diversion compared to the observed (GPM) rain rate, suggesting that once the peak intensification phase of the TC is reached, the model forecasted a large overestimation in rainfall estimation compared to observation (GPM). These aspects of enhanced rainfall situation in Yaas compared to Fani are exclusive regulated by local scale (rainfall efficiency) and large-scale factors (transport of VIMT and PWT). The supporting mechanisms attributed to these results are comprehensively justified through the analysis of rainfall efficiency terms in the following paragraph.

Figure 8b, d shows the LSPE and CMPE for Fani and Yaas. It is noted that there is strong coherent pattern existed during the first few hours (up to 18 h) due to the intensification process; however, it is evident that LSPE is intense in Yaas (190%) compared to Fani (130%). Thereafter, in the case of Fani of magnitude, LSPE (CMPE) is 135 (120%) is noted around 33 (30 h), suggesting a rapid intensification phase of the storm. In contrast, for Yaas, the maximum of LSPE (CMPE) is of the order of 190 (180%), around 45 (39) hours. Interestingly, LSPE (CMPE) maxima for Fani (Yaas) occurred 3

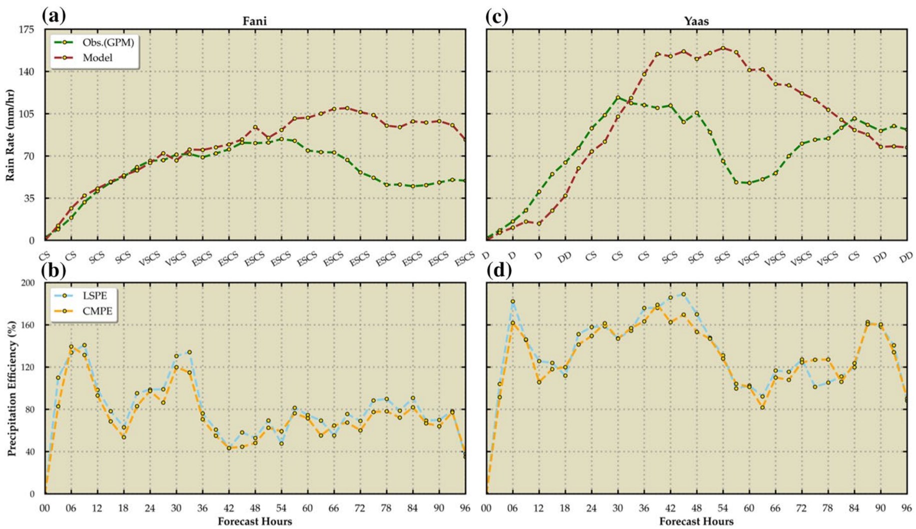

Fig. 8 LSPE (%), CMPE (%) and rain rate (mm/hr) for Fani (**a**–**b**) and Yaas (**c**–**d**) during the 96 forecast hour

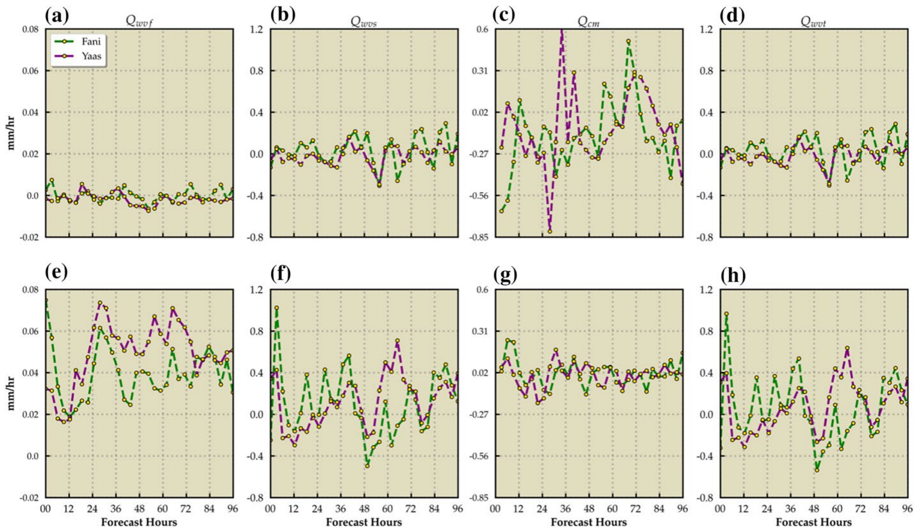

Fig. 9 Fani and Yaas precipitation efficiency individual terms (mm/hr): Q_{WVF} (water vapor flux convergence/divergence), Q_{WVS} (microphysical consumption of water vapor),), Q_{CM} (hydrometeor loss/gain), and Q_{WVT} (local atmospheric drying/moistening) for the integrated upper troposphere (600–100 hPa) (**a**–**d**) and lower troposphere (1000–500 hPa) (**e**–**h**) during the 96 forecast hours

(15) hours before their peak phases of intensification, suggesting the role of competing for local and large-scale environmental factors. In general, the majority of the forecast hours for both LSPE and CMPE, remained within 80% for Fani, whereas for Yaas, it has maintained strength with the lowest, around 120%. As the TCs enter their peak intensification phases, the gradual (sharp) decline in the LSPE (CMPE) 40 (40%) for Fani and 80 (95%) for Yaas is noted around 42 (63) forecast hours. This suggests that the mature phase of the TC has reached. Afterward, few fluctuations of LSPE (CMPE) but with less variability are noted in the case of Fani till the end of the forecast hour, suggesting the TC has attained its maximum rain-bearing saturation in the ESCS. In contrast, these variations are distinctly large in the case of Yaas, and they gradually increase with time and reach a maximum of 160 (160%) around 87 h, suggesting the TC's rainfall saturation is being modulated by some external processes. Another interesting aspect to note is that the duration of the peak intensification phase (i.e., VSCS) is only 18 h (60–70 h) in the case of Yaas, the LSPE and CMPE are the lowest (80–120%). However, it has shown the signature of amplification the system is decaying to SCS, suggesting that now the environment is under-saturated conditions. These under-saturated conditions might also be attributed due to the TC being closest to the coast and making landfall at 84 h. This aspect is also discussed in detail in the following section. Results, in general, suggest CMPE (local scale) is being dominated by LSPE (large-scale transport) in the case of both TC. Throughout the 96 forecast hours, the average LSPE (CMPE) value for Fani is 79.26 (72.87%), and that for Yaas is 132.71 (129.11%). Results also clearly indicate that LSPE and CMPE have shown significantly larger values for Yaas as compared to Fani, suggesting the dominance of large-scale environmental variables over the microphysical variables facilitating the intense rainfall scenario.

4.6.1 Individual terms of precipitation efficiency

The aforementioned results suggest that wet advection of water vapor through large-scale factors is the dominant mechanism amplifying the LSPE and CMPE in TCs. Further, a comprehensive diagnostic analysis of the relative contribution of individual terms of PE impacting Fani and Yaas is discussed. The time-series of 300 km area-averaged individual terms (Eqs. 3, 5, 6, 7, 8) contributing to LSPE and CMPE integrated over the lower (1000–500 hPa) and upper (600–100 hPa) troposphere are presented in Fig. 9a–h.

The moisture flux convergence ($Q_{WVF} > 0$) (Fig. 9a, e) has shown significant variation throughout the forecast hours for both Fani (Yaas) and ranging from −0.01 to 0.075 (−0.01 to 0.074 mm/hr) in the lower integrated level (1000–500 hPa) (Fig. 9e) as compared to upper integrated level (600–100 hPa) (Fig. 9a). Maxima of Q_{WVF} 0.06 (0.074 mm/hr) in Fani (Yaas) is limited to the lower level (1000–500 hPa), suggesting that the copious rainfall in both the TCs has been derived from the moist-convection associated with this moisture flux convergence. As the forecast proceeds, a gradual (intense) moisture flux convergence in Fani (Yaas) of mean value 0.04 (0.06 mm/hr) is noted during 24 to 72 h at the lower levels suggesting the peak phases of TCs. Afterward, Q_{WVF} remains fluctuating within 0.03 to 0.05 mm/hr for both TCs, a gradual (sharp) decrease in Q_{WVF} reaching 0.03 (0.04 mm/hr) around 78 h suggesting the decaying phase of intensification in the TCs. Upper-level Q_{WVF} has not shown much variation, and it varies around −0.0001 (−0.002 mm/hr) for Fani (Yaas) throughout the forecast hour, connotating a moderate(intense) upper-level divergence. Throughout the 96 forecast hours, the average value of Q_{WVF} is 0.03 (0.045 mm/hr) for Fani (Yaas), suggesting Yaas has experienced stronger vapor flux convergence as compared to Fani in the lower levels. This intense Q_{WVF} is one of the key factors facilitating the heavy rainfall in Yaas compared to Fani. Figure 9b, f shows the net amount of microphysical consumption of water vapor (Q_{WVS}) for Fani and Yaas at upper and lower levels. Except for the initial 12 h, both Fani (Yaas) have shown Q_{WVS} in the range −0.36 to 0.6 (−0.45 to 0.75 mm/hr) throughout the forecast duration, and maxima of Q_{WVS} reaches during their peak phase of intensification in the lower levels. Overall, Fani (Yaas) has shown Q_{WVS} around 0.08 (0.13 mm/hr) during the 96 h, suggesting the vigorous consumption (utilization) of water vapor in producing the rainfall and PE leading to atmospheric drying in the lower level only. (Fig. 9d, h).

These findings are further supported by the results of hydrometeor convergence ($Q_{CM} > 0$)/divergence ($Q_{CM} < 0$) (Fig. 9c, g), where it is noted that throughout the 96 forecast hours, Fani (Yaas) has shown gradual (intense) hydrometeor divergence/gain reaching Q_{CM} up to −0.10 (−0.128 mm/hr) in the upper levels as a consequence of intense low-level vapor flux convergence (Q_{WVF}) (Fig. 9a, e) and microphysical consumption of vapor (Q_{WVS}) (Fig. b, f). As the forecast proceeds, a hydrometeor divergence/gain reaching up to −0.42 (−0.8 mm/hr) is noted for both the Fani (Yaas) around 30 (27) hours (Fig. 9b, f), designating the intense conversion of the vapor to solid-phase hydrometeors. Thereafter, a sharp decrease in hydrometeor divergence/gain reaching up to 0.01 (0.6 mm/hr) has been shown by both the storms Fani (Yaas) phases around 39 (45) hours, suggesting the saturation of the process leading to solid hydrometeor gain. After 48 h, some obvious fluctuations in the range −0.3 to −0.01 mm/hr are noted in both these TCs, followed by a decrease in hydrometeor divergence reaching up to 0.5(~0.3 mm/hr) in Fani (Yaas) around 72 h suggesting the post intensification phases of both these TCs. Overall, Fani (Yaas) has shown a moderate (dominant) hydrometeor divergence/gain in terms of solid hydrometeor (e.g., snow and graupel) (Fig. 5b, c) in the upper levels reaching an average value up to −0.1 (−0.13 mm/hr) suggesting a moderate(intense) contribution of Q_{CM} in the denominator of PE which has led to lower (higher) magnitudes of LSPE and CMPE in Fani (Yaas). It is also noted that in the lower levels, Q_{CM} ranges from −0.01 to 0.2 mm/hr with an average of 0.004 (0.007 mm/hr) throughout the 96 forecast hours in Fani (Yaas), suggesting moderate (intense) hydrometeor convergence/loss. It suggests that Q_{CM} of lower integrated level has not shown significant variation suggesting that most of the solid hydrometeor formation is limited above 600 hPa and has little impact in modulating the rainfall.

The local atmospheric drying ($Q_{WVT} > 0$)/moistening ($Q_{WVT} < 0$) (Fig. 9d, h) has shown significant variation throughout the forecast hours for both Fani (Yaas) in the range −0.53 to 0.96 (−0.3 to 0.64 mm/hr). As the forecast proceeds, the maxima of Q_{wvt} is 0.46 (0.69 mm/hr) for Fani (Yaas) around 36 (60) hours which coincides with the respective peak phases of intensification in the lower troposphere. Afterward, Fani (Yaas) experienced a sharp (gradual) decrease in Q_{WVT}, reaching −0.28 (0.35 mm/hr) at the end of the forecast hour. The average value of Q_{WVT} for Fani (Yaas) is 0.04 (0.11 mm/hr) throughout the forecast duration, suggesting Yaas has shown atmospheric drying, particularly at the lower levels compared to Fani. Such variations in atmospheric drying are not found in the upper-tropospheric level of both of TCs, that's the reason the impact due to lower-level drying for a short duration is minimal, suggesting upper-level cold-rain process dominating the rain-making mechanisms in these TC. Overall, moderate (intense) drying (moistening) of magnitude 0.03(−0.28 mm/hr) have been noted in Fani (Yaas) throughout the 96 forecast hours.

The water vapor convergence($Q_{WVF} < 0$) and hydrometeor gain/divergence ($Q_{CM} < 0$), which account for a significant amount of the water vapor supply (Mao et al. 2017), have shown an overall dominance in the case of Yaas compared to Fani, suggesting the local increase in hydrometeors ($Q_{CM} < 0$) in upper integrated level consumed a lot of water vapor. It is clear that the lower tropospheric convergence of water vapor in Yaas is more intense than that of Fani, which corresponded to the higher Q_{WVF}, LSPE, and CMPE. Due to the high correlation between the cloud hydrometeors mixing ratio and updraft, it has led to intense convection in Yaas and consequently produced higher rainfall. Previous studies (Feng and Shu 2018; Huang et al. 2014; Gao and Tao 2005; Shu et al. 2018) suggest that the VIMFT is related to the interaction between the prevalent synoptic-scale processes and the storm's internal dynamics; therefore, the large magnitude of VIMFT in Yaas supporting our hypothesis that the large-scale processes are the primary reason behind the higher LSPE, CMPE and rainfall in Yaas compared to Fani. The minimal signatures of key parameters (i.e., Q_{WVS}, Q_{WVT}, and Q_{WVF}) in the upper levels are noted for both the TCs. However, the influence of individual components at the lower levels in Yaas (VSCS) is evident and plays a crucial role in the enhanced rainfall compared to Fani being ESCS.

5 Conclusions

The major thrust of this research work is to provide insight into the contrasting rainfall characteristics of two pre-monsoon TCs (i.e., Fani and Yaas) that have severely impacted the east coast of India. The purpose is to investigate the typical characteristics of the TCs in terms of track, intensification process, and rainfall. Further, the aim is to examine how rainfall is regulated through key precipitation efficiency mechanisms in these two TCs. In general, the model forecast captures intensity, intensification process, and track of the TCs reasonably well. However, as far as rainfall is concerned, it is noted that the model over-predicted the rainfall, particularly when TCs reaches their mature phase, but the pattern of rainfall magnitudes is in coherence with the storm intensification process supported by rainfall efficiency mechanisms. Further, we have noted that benchmark dynamical and thermodynamical processes (e.g., vertical updraft, radial wind, tangential wind, and diabatic heating) have shown robust magnitudes validating its stronger intensity in Fani (ESCS) as compared to Yaas (VSCS). In contrast, we have found that the large-scale processes (e.g., VIMFT and low-level-convergence are among the critical environmental parameters which have largely influenced the rainfall characteristics of Yaas as compared to Fani. One of the reasons attributed to this outcome, is the occurrence of Yaas closer to the monsoon onset time, facilitating intense incursion of VIMF and PWT through monsoon low-level jet to the TC.

Further, in-depth investigations are carried out to justify the reasons for a higher amount of rainfall in Yaas compared to Fani through the rainfall efficiency mechanism. In general, it is found that both CMPE and LSPE work in tandem in determining the rainfall for both the TCs. Further, this pattern is in coherence with the intensification of the TCs. However, it is evident that LSPE contributed through the large-scale incursion of moisture is dominated in the case of Yaas compared to Fani. This has facilitated the unprecedented accumulation of moisture and PWT in Yaas, in spite of a weaker TC compared to Fani. The magnitude of LSPE is too large for Yaas (100–190%) compared to Fani (70–140%), impacting directly model rainfall amount in respective TCs. It is also clearly seen that both LSPE and CMPE values have gradually decreased once TCs reached their peak stage, suggesting the mature phase of the TC with the saturated condition.

Examining the rainfall efficiency individual terms, it is noted that, Yaas having intense moisture flux convergence in the lower level (1000–500 hPa) has led to more solid hydrometeor gain/divergence in the upper level (600–100 hPa). This gain of hydrometeor is reflected as moderate (intense) atmospheric drying in the case of Fani(Yaas), which suggests large consumption of water vapor at a lower integrated level throughout the forecast hour. Except for solid hydrometeor gain, other processes of PE individual terms have shown relatively small signatures in the upper integrated level suggesting a little impact on the cold-rain process and hence on PE of the TCs. Being in the denominator of the PE equation, all these processes have contributed to increasing the PE in the case of Yaas as compared to Fani. Besides, the co-occurrence of enhanced upper integrated level solid hydrometeor gain and lower-level atmospheric drying in the case of Yaas as compared to Fani suggest their mutual modulation. The enhanced atmospheric drying in the case of Yaas has led to a decrease in the PE, but at the same time, the stronger lower tropospheric vapor flux convergence in the TC has dominated to enhance the LSPE. In the case of Yaas, upper-tropospheric solid hydrometeor gain and lower tropospheric microphysical consumption of water vapor are higher and trying to regulate CMPE, but the numerator term being the rainfall rate has a higher magnitude compared to denominator terms (i.e., hydrometeor loss/gain and microphysical consumption), leading to higher magnitude of CMPE compared to Fani. This mechanism has led to copious rainfall by facilitating the cold-rain forming processes in Yaas compared to Fani, even though Fani is a stronger TC.

Overall, TC rainfall distribution may be controlled by many factors and would vary during the period of landfall. Yass has produced heavy rainfall over a large area, including Odisha and West Bengal due to the effective coupling of ambient synoptic systems and mesoscale precipitation efficiency processes. Therefore, it can be concluded that rainfall differences between the two TCs are strongly related to moisture modulations and rainfall production and the precipitation efficiency and associated processes, particularly within 300 km from the TC center. These results also suggest that relatively weaker TCs can still produce heavy rain and devastation. A concise view of overall findings and the competence of dynamical, microphysical, and thermodynamical parameters on rainfall for two

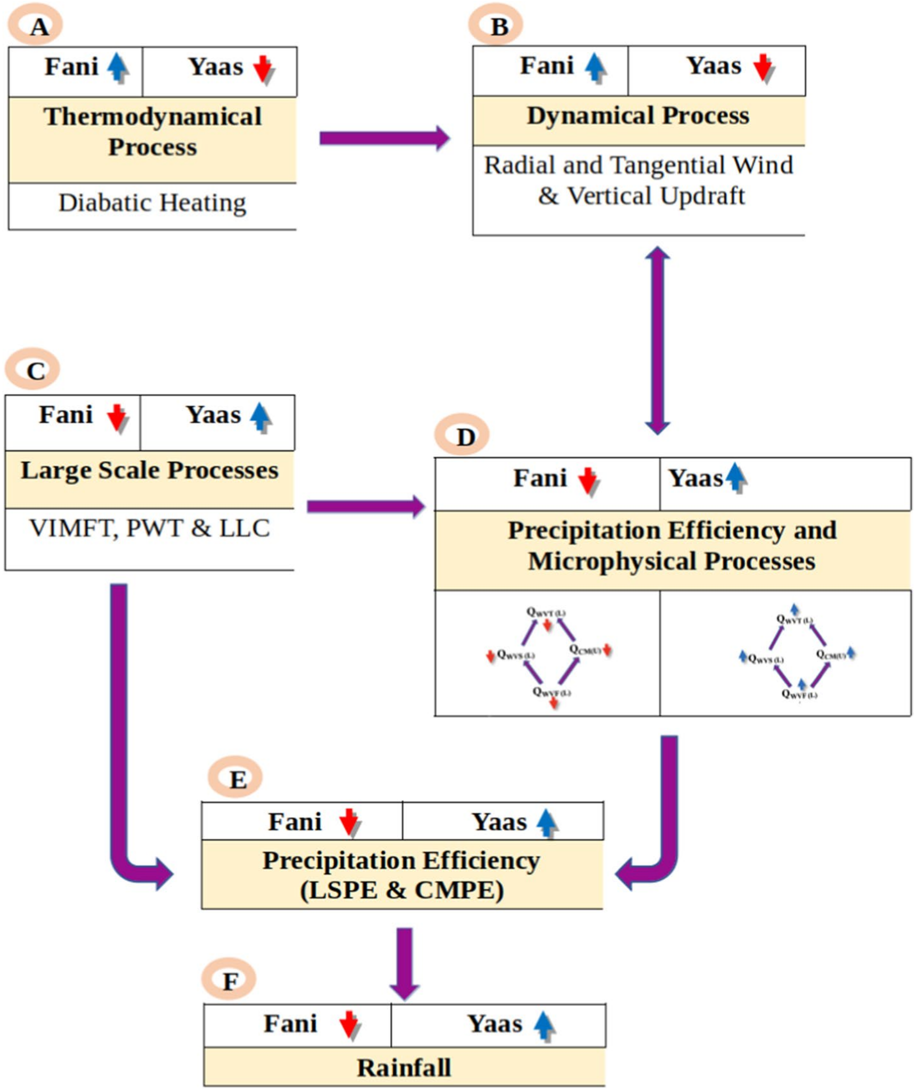

Fig. 10 Schematic representing relative competence of the dynamical, microphysical, and thermodynamical processes throughout the 96 forecast hours for the TCs Fani and Yaas. Blue upward and red downward arrows represent the surplus and deficit of the corresponding processes, respectively. Q_{WVF}(L), Q_{WVS}(L), Q_{CM}(U), and Q_{WVT}(L) designate the moisture flux convergence, water vapor consumption, hydrometeor loss, and atmospheric drying. L and U stands for integrated lower (1000–500 hPa) and upper (600–100 hPa) troposphere level. VIMFT, PWT, LLC, LSPE, and CMPE stand for vertically integrated moisture flux transport, precipitable water, low-level convergence, large-scale precipitation efficiency and cloud microphysical precipitation efficiency, respectively

contrasting TCs over the BoB region is presented in Fig. 10. So far as the challenge of rainfall forecast associated with landfalling TCs is concerned, this should draw as much attention. This study reveals a possible mechanism of how weak TCs producing heavy rainfall deserves as much attention as strong TCs in operational forecasting and research. The prediction of rainfall during TCs landfall in terms of its intensity, distribution, and spatiotemporal variability is highly challenging over the NIO region, and the findings of this study will facilitate a better understanding of precipitation modulating processes that have direct consequences on operational forecasting models.

Supplementary Information The online version contains supplementary material available at https://doi.org/10.1007/s11069-022-05439-z.

Acknowledgments The authors are grateful to the Indian Institute of Technology Bhubaneswar for providing the necessary infrastructure to carry out this research work. We are also grateful to the Council of Scientific and Industrial Research (CSIR) for providing financial support for carrying out this research work. In addition, we are grateful to the Scientific and Engineering Research Board (SERB), Department of Science and Technology (DST) and New Venture Fund for their support. We extend our sincere gratitude to the India Meteorological Department (IMD) for providing data sets. We are grateful to NCEP-NCAR, NASA-GPM, and NOAA for providing the WRF model, rainfall, and SST data for carrying out this research.

Author's Contribution VV executed the simulation, designing of experiments, carried out the detailed investigation and participated in manuscript writing. SP conceived the research idea, helped in designing the experiments, participated in analyzing results and manuscript drafting.

Funding Authors are grateful to Indian Institute of Technology Bhubaneswar, Council of Scientific and Industrial Research (CSIR), India and New Venture Fund for their funding support.

Declarations

Conflict of interest The authors do not have any competing interests.

References

Auer AHJ, Marwitz JD (1968) Estimates of air and moisture flux into hailstorms on the High Plains. J Appl Meteorol 7:196–198

Baisya H, Pattnaik S, Chakraborty T (2020) A coupled modeling approach to understand ocean coupling and energetics of tropical cyclones in the Bay of Bengal basin. Atmos Res 246:105092

Balaji M, Chakraborty A, Mandal M (2018) Changes in tropical cyclone activity in North Indian Ocean during satellite era (1981–2014). Int J Climatol 38:2819–2837

Bell MM (2017) Extreme precipitation from tropical cyclones Invited Review at the Sixth international workshop on monsoons (IWM-VI). World Meteorol Org 13–17 Singapore

Bougeault P, Lacarrere P (1989) Parameterization of orography-induced turbulence in a mesobeta-scale model. Mon Weather Rev 117(8):1872–1890

Braham RR (1952) The water and energy budgets of the thunderstorm and their relation to thunderstorm development. J Meteorol 9:227–242

Brown BR, Bell MM, Frambach AJ (2016) Validation of simulated hurricane drop size distributions using polarimetric radar. Geophy Res Lett 43(2):910–917

Campos E, Wang J (2015) Numerical simulation and analysis of the April 2013 Chicago floods. J of Hydrol 531:454–474

Carbone RE (1982) A severe frontal rainband. Part I: Stormwide hydrodynamic structure. J Atmos Sci 39:258–279

Chakraborty T, Pattnaik S, Vishwakarma V, Dey S (2021) Spatio-temporal variability of pre-monsoon convective events and associated rainfall over the State of Odisha (India) in the recent decade. Pure Appl Geophys 178:4633–4649. https://doi.org/10.1007/s00024-021-02886-w

Chong M, Hauser D (1989) A tropical squall line observed during the COPT 81 experiment in West Africa. Part II: Water budget. Mon Weather Rev 117(4):728–744
Collins WD, Rash PJ, Boville BA, Hack JJ, McCaa JR, Williamson DL, Kiehl JT, Briegleb B (2004) Description of the NCAR Community Atmosphere Model (CAM 3.0), NCAR Technical Note
Cotton WR, Lin MS, McAnelly RL, Tremback CJ (1989) A composite model of mesoscale convective complexes. Mon Weather Rev 117(4):765–783
Doswell CA, Brooks HE, Maddox RA (1996) Flash flood forecasting: an ingredients-based methodology. Weather Forecasting 11:560–581
Fankhauser JC (1988) Estimates of thunderstorm precipitation efficiency from field-measurements in Ccope. Mon Weather Rev 116:663–684
Feng X, Shu S (2018) How do weak tropical cyclones produce heavy rainfall when making landfall over China. J Geophys Res Atmos 123(21):11–830
Ferrier BS, Simpson J, Tao W (1996) Factors responsible for precipitation efficiencies in midlatitude and tropical squall simulations. Mon Weather Rev 124:2100–2125
Fierro AO, Rogers RF, Marks FD, Nolan DS (2009) The impact of horizontal grid spacing on the microphysical and kinematic structures of strong tropical cyclones simulated with the WRF-ARW model. Mon Weather Rev 137(11):3717–3743
Frank WM, Ritchie EA (1999) Effects of environmental flow upon tropical cyclone structure. Mon Weather Rev 127(9):2044–2061
Frank WM, Ritchie EA (2001) Effects of vertical wind shear on the intensity and structure of numerically simulated hurricanes. Mon Weather Rev 129(9):2249–2269
Fritsch JM, Chappell CF (1980) Numerical prediction of convectively driven mesoscale pressure systems. Part I: Convective parameterization. J Atmos Sci 37:1722–1733
Gao S, Li X (2011) The dependence of precipitation efficiency on rainfall type in a cloud-resolving model. J Geophys Res-Atmos 116:D21207. https://doi.org/10.1029/2011JD016117
Gao ST, Cui XP, Zhou YS, Li XF (2005) Surface rainfall processes as simulated in a cloud-resolving model. J Geophys Res Atmos 110:D10. https://doi.org/10.1029/2004jd005467
Grell GA (1993) Prognostic evaluation of assumptions used by cumulus parameterizations. Mon Weather Rev 121:764–787
Guzman O, Jiang H (2021) Global increase in tropical cyclone rain rate. Nature Commun 12:5344
Hanesiak JM, Stewart RE, Szeto KK, Hudak DR, Leighton HG (1997) The structure, water budget, and radiational features of a high-latitude warm front. J Atmos Sci 54:1553–1573
Hazelton A, Rogers R, Hart R (2017) Analyzing simulated convective bursts in two Atlantic Hurricanes. part i: burst formation and development. Mon Weather Rev 145:3073–2094. https://doi.org/10.1175/MWR-D-16-0267.1
Hendricks EA, Jin Y, Moskaitis JR, Doyle JD, Peng MS, Wu CC, Kuo HC (2016) Numerical simulations of Typhoon Morakot (2009) using a multiply nested tropical cyclone prediction model. Weather Forecast 31:627–645
Heymsfield GM, Schotz S (1985) Structure and evolution of a severe squall line over Oklahoma. Mon Weather Rev 113:1563–1589
Hobbs PV, Matejka TJ, Herzegh PH, Locatelli JD, Houze JRA (1980) The mesoscale and microscale structure and organization of clouds and precipitation in midlatitude cyclones. I: a case study of a cold front. J Atmos Sci 37:568–596
Huang HL, Yang MJ, Sui CH (2014) Water budget and precipitation efficiency of Typhoon Morakot (2009). J Atmos Sci 71(1):112–129
Huang W, Feng S, Chen J, Chen F (2015) Physical mechanisms of summer precipitation variations in the Tarim Basin in Northwestern China. J Clim 28(9):3579–3591
Huffman GJ, Bolvin DT, Braithwaite D, Hsu K, Joyce R, Xie P, Yoo SH (2015) NASA global precipitation measurement (GPM) integrated multi-satellite retrievals for GPM (IMERG). Algorithm Theoretical Basis Document (ATBD) Version 4:26
IMD (2019) Extremely Severe Cyclonic Storm 'FANI' over Bay of Bengal: A Report. retrieved from http://www.rsmcnewdelhi.imd.gov.in (Accessed on 30 October 2021)
IMD (2021) Very Severe Cyclonic Storm 'YAAS' over Bay of Bengal: A Report. retrieved from http://www.rsmcnewdelhi.imd.gov.in (Accessed on 30 October 2021)
Jones C, Weare BC (1996) The role of low-level moisture convergence and ocean latent heat fluxes in the Madden and Julian oscillation: An observational analysis using ISCCP data and ECMWF analyses. J Clim 9(12):3086–3104
Kain JS (2004) The Kain-Fritsch convective parameterization: an update. J Appl Meteorol 43:170–181
Kirshbaum DJ, Grant ALM (2012) Invigoration of cumulus cloud fields by mesoscale ascent. Q J R Meteorol Soc 138(669):2136–2150

Konrad CE, Perry LB (2010) Relationships between tropical cyclones and heavy rainfall in the Carolina region of the USA. Int J Climatol: J Royal Meteorol Soc 30(4):522–534

Krishna KM, Rao SR (2009) Study of the intensity of super cyclonic storm GONU using satellite observations. Int J Appl Earth Obs Geoinf 11(2):108–113

Kuo HL (1974) Further studies of the parameterization of the influence of cumulus convection on large-scale flow. J Atmos Sci 31:1232–1240

Li X, Sui CH, Lau KM (2002) Precipitation efficiency in the tropical deep convective regime: a 2-D cloud resolving modeling study. J Meteorol Soc Japan 80:205–212

Lim KSS, Hong SY (2010) Development of an effective double-moment cloud microphysics scheme with prognostic cloud condensation nuclei (CCN) for weather and climate models. Mon Weather Rev 138:1587–1612

Lipps FB, Hemler RS (1986) Numerical simulation of deep tropical convection associated with large-scale convergence. J Atmos Sci 43:1796–1816

Lonfat M (2004) Tropical cyclone rainfall: An observational and numerical study of the structure and governing physical processes. University of Miami

McCaul EW, Cohen C, Kirkpatrick C (2005) The sensitivity of simulated storm structure, intensity, and precipitation efficiency to environmental temperature. Mon Weather Rev 133:3015–3037

Ng EK, Chan JC (2012) Interannual variations of tropical cyclone activity over the north Indian Ocean. Int J Climatol 32(6):819–830

Ooyama KV (1982) Conceptual evolution of the theory and modeling of the tropical cyclone. J Royal Meteor Soc Japan 60:369–379

Palmén E, Newton CW (1969) Atmospheric circulation systems: their structure and physical interpretation. Academic press, New York, NY

Pattnaik S, Krishnamurti T (2007) Impact of cloud microphysical processes on hurricane intensity, part 2: Sensitivity experiments. Meteorol Atmos Phys 97:127–147

Pattnaik S, Inglish C, Krishnamurti TN (2011) Influence of rain rate initialization, cloud microphysics and cloud torques on Hurricane Intensity. Mon Weather Rev 139:627–649

Paulson CA (1970) The mathematical representation of wind speed and temperature profiles in the unstable atmospheric surface layer. J Appl Meteorol 9:857–861

Rai D, Pattnaik S (2018) Sensitivity of tropical cyclone intensity and structure to planetary boundary layer parameterization. Asia Pacific J Atmos Sci 54:473–488

Rai D, Pattnaik S, Rajesh PV, Hazra V (2019) Impact of high-resolution sea surface temperature on tropical cyclone characteristics over the Bay of Bengal using model simulations. Meteorol Appl 26(1):130–139

Shapiro LJ (1983) The asymmetric boundary layer flow under a translating hurricane. J Atmos Sci 40:1984–1998

Shu S, Wu L (2009) Analysis of the influence of Saharan air layer on tropical cyclone intensity using AIRS/Aqua data. Geophys Res Lett. https://doi.org/10.1029/2009GL037634

Shu S, Zhang F, Ming J, Wang Y (2014) Environmental influences on the intensity changes of tropical cyclones over the western North Pacific. Atmos Chem and Phys 14(12):6329–6342

Shu S, Feng X, Wang Y (2018) Essential role of synoptic environment on rainfall distribution of landfalling tropical cyclones over China. J Geophys Res-Atmos 123(20):11–285

Skamarock WC, Klemp JB, Dudhia J, Gill DO, Barker DM, Duda MG, Huang XY, Wang W, Powers JG (2008) A description of the advanced research WRF Version 3. Technical Report NCAR/TN-475+STR. National Centre for Atmospheric Research, Boulder, CO

Sui CH, Li X, Yang MJ, Huang HL (2005) Estimation of oceanic precipitation efficiency in cloud models. J Atmos Sci 62:4358–4370. https://doi.org/10.1175/JAS3587.1

Sui CH, Li X, Yang MJ (2007) On the definition of precipitation efficiency. J Atmos Sci 64:4506–4513. https://doi.org/10.1175/2007JAS2332.1

Tewari M, Chen F, Wang W, Dudhia J, LeMone M, Cuenca RH (2004) Implementation and verification of the unified NOAH land surface model in the WRF model, In 20th conference on weather analysis and forecasting 16th conference on numerical weather prediction, pp 11–15

Wang CC, Kuo HC, Johnson RH, Lee CY, Huang SY, Chen YH (2015) A numerical study of convection in rainbands of Typhoon Morakot (2009) with extreme rainfall: roles of pressure perturbations with low-level wind maxima. Atmos Chem Phys 15:11097–11115

Weisman ML, Klemp JB (1982) The dependence of numerically simulated convective storms on vertical wind shear and buoyancy. Mon Weather Rev 110:504–520

Xu J, Wang Y (2010) a) Sensitivity of tropical cyclone inner-core size and intensity to the radial distribution of surface entropy flux. J Atmos Sci 67(6):1831–1852

Xu H, Zhai G, Li X (2017) Precipitation efficiency and water Budget of Typhoon Fitow (2013): a particle trajectory study. J Hydrometeorol 18(9):2331–2354

Yanai M, Esbensen S, Chu JH (1973) Determination of bulk properties of tropical cloud clusters from large-scale heat and moisture budgets. J Atmos Sci 30(4):611–627
Yang S, Tang X, Zhong S, Chen B, Zhou Y, Gao S, Wang C (2019) Convective bursts episode of the rapidly intensified Typhoon Mujigae (2015). Adv Atmos Sci 36(5):541–556